



Formation mechanism and stability of austenitic islands in carbides in a Ni-Cr-Fe based high-temperature austenitic alloy undergoing carburization

Shipeng Shu^{a,*}, Xiaobing Hu^a, Maryam Kazemzadeh-Atoufi^a, Tao Liu^{a,b}, Anyu Shang^a, Mark B. Davis^d, Robin Ziebarth^e, Sandeep Dhingra^e, Robert D. Morgan^e, Yao Du^d, Peter W. Voorhees^a, David N. Seidman^{a,c}

^a Northwestern University, Department of Materials Science and Engineering, 2220 Campus Drive, Evanston, IL 60208 USA

^b College of Materials Science and Engineering, Chongqing University, Chongqing 400044, PR China

^c Northwestern University Center for Atom-Probe Tomography, 2220 Campus Drive, Evanston, IL 60208 USA

^d Dow Chemical Company, Freeport, TX 77541 USA

^e Dow Chemical Company, Midland, MI 48674 USA

ARTICLE INFO

Article history:

Received 3 December 2020

Revised 3 February 2021

Accepted 6 February 2021

Available online 18 February 2021

Keywords:

High-temperature alloys

Phase transformation

Analytical electron microscopy

Atom-probe tomography

Dual-beam FIB tomography

ABSTRACT

We investigate a phase transformation in a Ni-Cr-Fe-based high-temperature alloy during the technologically important carburization process, with multi-length scale experimental techniques. The study focuses on the formation and stability of novel austenitic islands formed within carbide structures during the $M_{23}C_6$ to M_7C_3 phase-transformation. We demonstrate that the austenitic islands nucleate near the $M_{23}C_6/M_7C_3$ transformation front, from a supersaturation of metal atoms in the $M_{23}C_6$ -carbide as M_7C_3 grows. After formation, the austenitic islands equilibrate their composition with the matrix temporally but remain relatively stable inside the carbides due to their large sizes (a few hundred nanometers in diameter) and a weak Gibbs-Thomson effect.

© 2021 Acta Materialia Inc. Published by Elsevier Ltd. All rights reserved.

Ni-Cr-Fe-based austenitic alloys with a high Cr content exhibit excellent high-temperature corrosion and creep resistance and are widely used in extreme environments [1–5]. These high-temperature alloys are the materials of choice for a modern pyrolysis furnace, which is the main facility used in the petrochemical industry to produce ethylene, arguably the most important basic chemical building block with an annual global production of ~ 200 million metric tons with market size of USD 146.3 billion [6]. Therefore, understanding and further improving the properties of the Ni-Cr-Fe-based austenitic alloys is crucial for this important industry. It has been well documented that when these alloys are subjected to elevated temperatures (700 – 1100°C) and a high carbon activity environment, such as in pyrolysis furnaces [7–9], carbon can diffuse from the surface to the alloy's interior, leading to severe carburization [10,11]. The carburization phenomenon is characterized by the growth of existing Cr-rich carbides along interdendritic channels, formation of new carbides, and transformation of $M_{23}C_6$ -precipitates to more stable M_7C_3 -precipitates at

a high carbon activity; M consists of metallic elements such as Cr, Fe, etc. [12–14]. Formation of a high-volume fraction of Cr-rich carbide-precipitates often leads to the deterioration of the mechanical properties of an alloy [15,16]. Therefore, extensive studies of the microstructural evolution of the carbide-precipitates are performed to understand the formation mechanism of the carbide-precipitates and the kinetics of carburization [10,17,18]. Interestingly, prior studies demonstrated that after carburization, the M_7C_3 -carbide precipitates often contain a significant amount of an austenitic phase as small precipitates [10,18], thereby forming a complex hierarchical precipitate structure. To differentiate them from the common second-phase precipitates formed directly in the matrix, such as Cu precipitation in Fe [19,20], we refer to them henceforth as *austenitic islands* (AIs). These unusual islands are akin to the core-shell precipitate-structures observed in some Al alloys [21–23], but here the islands consist of the matrix phase. The structure of the matrix phase precipitating in the second-phase precipitates has been previously observed in driven systems [24], such as a Cu-12 at.%Fe alloy irradiated by 1.8 MeV Kr^+ ions at 350°C, where the Cu islands formed in the Fe precipitates [25]. The stabilization of the structure was shown, however, to be a result of the irradiation modifying the effective capillary length [26],

* Corresponding author.

E-mail address: spshu@northwestern.edu (S. Shu).

Table 1

Composition of the alloy in wt.% and at.%, measured by inductivity-coupled argon plasma atomic-emission spectrometry (ICAP-AES) at Genitest, Inc (Montréal, QC).

	Fe	Cr	Ni	Nb	Mn	C	Si	P	S
wt.%	15.73	35.53	44.47	1.10	1.02	0.47	1.85	0.016	0.004
at.%	15.15	36.76	40.76	0.64	1.00	2.11	3.54	0.028	0.007

which is not applicable to our system. Another example of such structures was observed in Ni-based superalloys, characterized by the γ (face-centered cubic, FCC) matrix with γ' (L1₂) precipitates that contain embedded γ precipitates [27,28]. Such sub-structures within precipitates can affect the creep properties [29], crack propagation [10], and coarsening resistance of the second phase precipitates [28], etc. Additionally, they also reveal valuable information related to phase transformation mechanisms in a non-conservative system with a continuous flux of carbon atoms coming from the environment, and therefore they need be thoroughly understood. We utilize multiscale characterization techniques, including scanning electron microscopy (SEM), transmission electron microscopy (TEM), atom-probe tomography (APT), and focused ion-beam (FIB) tomography to obtain information on the Al size evolution, spatial relationships with the surrounding carbide precipitates, chemical compositions, and 3D connectivity with the matrix. Combining the experimental observations with thermodynamic analyses, we obtain the formation mechanism and stability of the Als.

A 10 mm \times 10 mm \times 3 mm sample coupon of a Cr-Ni-Fe-based high-temperature alloy (35 wt.% Cr/45 wt.% Ni), used in hydrocarbon cracking furnaces (composition listed in Table 1), was carburized in a 98% H₂/2% CH₄ (volume fraction) atmosphere at 1000°C for 98 h. During the process, carbon atoms diffuse from the surface into the bulk, leading to an increased carbon activity in the alloy. Resulting from the diffusion process, a carbon content gradient is expected (highest at the surface), which is confirmed by DICTRA calculations (see Supplementary Information, SI). The carbon content gradient leads to different types of carbides at different depths, with M₃C₂ being stable close to the surface, M₂₃C₆ at the center of the coupon, and M₇C₃ in between [30]. Cross-sections of the carburized coupons were prepared by first sectioning the sample, then mechanically grinding and polishing the cross-section, with a final finish achieved by vibratory polishing with 0.05 μ m colloidal silica slurry. Fig. 1a displays an SEM micrograph of the cross-section of the carburized alloy (surface at the top of the micrograph), which exhibits a large volume fraction of carbide-precipitates (darker gray contrast). The dashed line denotes the boundary between the transformed M₇C₃ (closer to the surface) and the remaining M₂₃C₆ (deeper into the bulk). Fig. 1b–d display the carbide structures at approximate depths of 200, 400, and 600 μ m beneath the surface. As the carburization involves inward diffusion of carbon atoms, which is time dependent, the actual carburization times for different depths of the sample are different. Using the microstructures of different depths of the same sample to discuss the evolution is equivalent to using different samples carburized for different times and looking at the same depth (see SI). Unmistakably, the Als are present at all three depths, but the dimensions of the islands vary. At depths of 600 μ m, where the M₇C₃/M₂₃C₆ transformation is occurring, the Als nucleate at the M₇C₃/M₂₃C₆ transformation front and they are relatively small because they are in the initial stages of nucleation and growth. The largest Als are detected at an intermediate depth of \sim 400 μ m, inside the fully transformed M₇C₃ carbides. At a depth of 200 μ m, the Als have the smallest dimensions compared to the other depths, suggesting that the Als are dissolving after their formation.

To examine the detailed structures of the Als and the surrounding M₇C₃/M₂₃C₆ carbide precipitates, we prepared a TEM sample

using the standard FIB lift-out technique [31], targeting a carbide structure in the interdendritic area with Als and the M₇C₃/M₂₃C₆ transformation front. Fig. 2a displays a high-angle annular dark-field (HAADF) micrograph taken with a probe-corrected JEOL ARM 200CF TEM, highlighting the distinct phases. The yellow-dashed lines depict the interface between the M₂₃C₆ carbide precipitates and the M₇C₃ grains (the transformation front); the red-dotted lines denote the grain boundaries (GBs) of different M₇C₃ grains; lastly, the blue dotted-lines mark the GBs in different M₂₃C₆ grains. Fig. 2b–g display energy dispersive X-ray spectroscopy (EDS) maps of the spatial distributions of the major elements in the alloy. Fig. 2a demonstrates that the M₂₃C₆ grains are surrounded by multiple M₇C₃ grains. The adjacent M₇C₃ and M₂₃C₆ grains do not exhibit a rational orientation relationship (OR). There are five isolated bright islands as revealed in the HAADF micrograph, enumerated by the numbers from 1 to 5. EDS maps demonstrate that islands 1 – 4 are Fe- and Ni-rich, similar in composition to the matrix, while island 5 is Nb-rich. Electron diffraction patterns (not displayed) confirmed that islands 1 – 5 are all FCC. The lattice parameters of the islands 1 – 4 are \sim 0.364 nm, consistent with the austenite matrix, and that of island 5 (\sim 0.464 nm) is consistent with NbC [32], which is present in the as-cast alloy (see SI). Note that the Als 1 to 4 all reside close to the M₂₃C₆/M₇C₃ heterophase boundaries, and specifically, Als 1 to 3 form at triple junctions. In the archival literature, two types of crystallographic orientation relationships (ORs) have been identified between the M₂₃C₆ carbide and the FCC matrix: cube-on-cube and a twin-related OR [33]. Austenitic island 1 has the classical cube-on-cube OR with the adjacent M₂₃C₆ grain, while islands 2 – 4 do not have a rational OR with M₂₃C₆. It is worthwhile noting that the interfacial morphologies of Als 3 and 4 are different on the M₂₃C₆ and M₇C₃ sides, which is consistent with an anisotropic interfacial free energy; that is, different values of the energies of the Al/M₂₃C₆ and Al/M₇C₃ heterophase interfaces. Surrounding the NbC, there is a Cr-Ni-Nb-Si-rich region, most likely the result of decomposition of NbC, which is unstable at 1000°C [8,18].

To determine accurately the compositions of the Als, multiple APT nanotips were prepared using the standard FIB lift-out method [34] at different depths. The APT nanotips were analyzed using a Cameca LEAP 5000XS tomograph, employing a picosecond ultraviolet (355 nm wavelength) laser (pulse energy set as 10 pJ) at a specimen temperature of 50 K. Further details concerning the LEAP 5000XS tomograph parameters and the reconstruction process is found in the SI. Results from three lift-outs taken at depths of 215 μ m, 420 μ m, and 505 μ m are reported. The reconstruction of one particular nanotip, lifted out at a depth of a 505 μ m, with both the Al and the adjacent M₇C₃ carbide is displayed in Fig. 3a. A concentration profile taken across the Al/M₇C₃ heterophase interface is presented in Fig. 3b, illustrating the distinct compositions of the M₇C₃ carbide and the Al. The M₇C₃ carbide is enriched in Cr, Fe and C, while the Al is characterized by high Ni, Fe, and Cr concentrations, with smaller concentrations of Si and Mn. Significant P segregation (peaks at \sim 0.5 at.%) at the Al/M₇C₃ heterophase interface is evident (note the bulk concentration of P is $<$ 0.03 at.%). To compare with the compositions of the surrounding matrix, the concentrations of the major elements (Ni, Fe, Cr) of the Als, measured by APT, and the matrix composition determined by both APT and SEM EDS analyses are compared in Fig. 3c. Surpris-

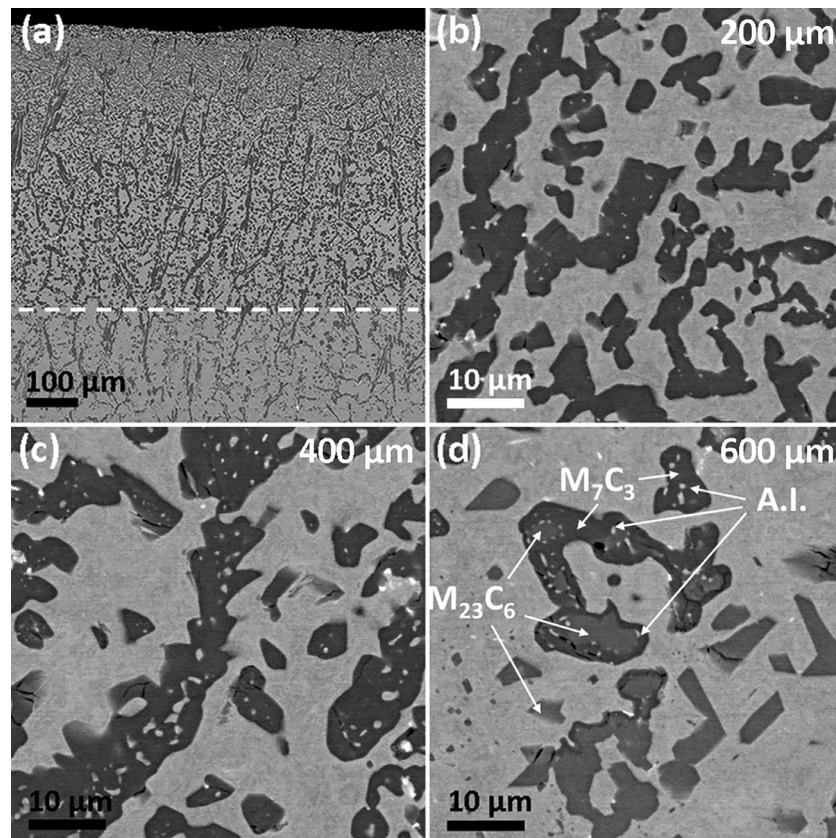


Fig. 1. SEM back-scattered electron (BSE) micrographs displaying the cross-sectional microstructures of the alloy, carburized in a 98% H₂/2% CH₄ (volume fraction) atmosphere at 1000°C for 98 h. The four micrographs display: (a) low-magnification overview with carbides (M₇C₃, M₂₃C₆), austenitic island microstructures at approximately (b) 200 μm; (c) 400 μm; and (d) 600 μm beneath the surface.

Table 2

Concentrations of major metallic elements in M₂₃C₆ and M₇C₃ carbides, measured by APT. For M₇C₃, the sample was lifted out close to the transformation front, at ~ 600 μm. For M₂₃C₆, the sample was lifted out at larger depth than the transformation front, at ~ 980 μm.

	Cr	Ni	Fe	Mn
M ₂₃ C ₆	64.61 ± 0.25	4.72 ± 0.12	6.29 ± 0.11	0.74 ± 0.06
M ₇ C ₃	64.05 ± 0.51	0.14 ± 0.19	6.42 ± 0.25	0.21 ± 0.20

ingly, the compositions of the AIs follow closely the trend of the composition evolution of the matrix as a function of depth. This observation is unexpected because in both the SEM and TEM micrographs, the AIs appear to be disconnected completely from the matrix. To determine the 3D spatial relationship of the carbides as well as the connectivity of the AIs and the matrix, FIB tomography was performed for one interdendritic carbide structure, which contains the M₂₃C₆/M₇C₃ transformation front, Fig. 4a. Fig. 4b–d exhibit the FIB tomography reconstruction, which indicates that the AIs are isolated, completely disconnected from the matrix, and populated close to the M₂₃C₆/M₇C₃ heterophase interface, confirming the SEM and TEM observations.

Based on the characterization results, we discuss the nucleation mechanism, evolution of the AIs, and the carbide transformation process. During carburization at a high carbon activity, M₂₃C₆ transforms to the more stable M₇C₃-phase. APT-measured carbide compositions indicate that the concentrations of elements consisting of M are different in the transformation product M₇C₃ and the original M₂₃C₆, Table 2. Most notably, Ni is much leaner in M₇C₃ compared to in M₂₃C₆. As a result, the excess non-carbide-forming metallic elements that are not accommodated by the newly formed M₇C₃ are rejected at the transformation front. This rejection of

M atoms can either supersaturate the M₂₃C₆-phase from its equilibrium composition, or segregate at the M₂₃C₆/M₇C₃ heterophase interface, leading to the nucleation of austenite. TEM EDS analysis reveals, however, no evidence of a compositional gradient in the M₂₃C₆ phase (see SI for details). Additionally, the fact that the AIs do not all have the cube-on-cube OR with the M₂₃C₆ phase suggests that the initial nucleation is not inside the M₂₃C₆ grains. Therefore, between the above-mentioned two possibilities, the second mechanism is more plausible.

GB triple junctions are the most energetically favorable sites for a nucleation process, and preferential nucleation at triple junctions are indeed observed, Fig. 2a. Once the initial AIs nucleate, further nucleation of other austenitic precipitates in the immediate vicinities is suppressed, and they distribute uniformly along the M₂₃C₆/M₇C₃ transformation front, consistent with an interfacial diffusion process, Fig. 1d. After the outer shell portion of the M₂₃C₆-precipitate/carbide is transformed to M₇C₃, carbon is still anticipated to diffuse rapidly into the carbide structure through the M₇C₃ GBs (red dotted-lines, Fig. 2a), thereby feeding the transformation front (yellow dashed line, Fig. 2a) and leading to its propagation. An example is displayed in Fig. 2a, where the phase boundary near AI 3 is in the process of bypassing the AI. Note the AIs are Cr-lean upon forming (Fig. 3b). Thus, it would be difficult for them to be later transformed to carbides (not enough carbide-forming metallic elements). After the transformation front bypasses completely the AIs, further interface propagation to the cores of the M₂₃C₆ carbides and the accompanying rejection of solute atoms are anticipated to nucleate new AIs along the migrating boundaries. This process leads to uniformly distributed austenitic precipitates inside the fully transformed M₇C₃ carbide (specifically for larger ones), consistent with our observations, Fig. 1b.

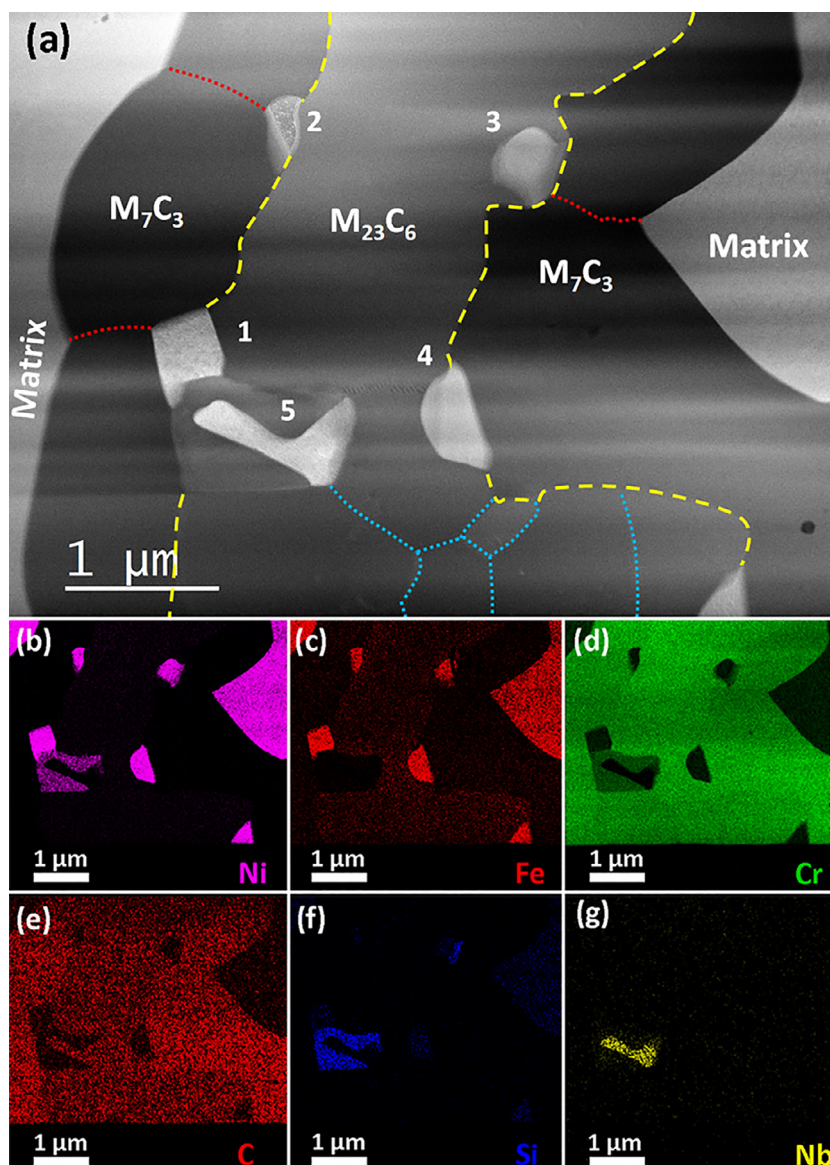


Fig. 2. (a) HAADF STEM micrograph displaying both M_7C_3 and $M_{23}C_6$ carbide-phases, four austenitic islands (marked as 1–4), and one NbC grain (marked as 5). The $M_7C_3/M_{23}C_6$ heterophase interface is delineated with yellow dashed lines. GBs within M_7C_3 and $M_{23}C_6$ are marked with red and blue dotted lines, respectively. (b–g) STEM EDS maps of the major alloying elements Ni, Fe, Cr, C, Si and Nb. Note that the grain boundaries display better contrast in the STEM bright-field micrograph, see SI. (For interpretation of the references to color in this figure legend, the reader is referred to the online version of this article.)

After the transformation of the carbides is complete, diffusion between the AIs and the matrix may still occur through the bulk M_7C_3 precipitates, which is slower, and along M_7C_3 grain boundaries (faster diffusion). This diffusion can lead to the equilibration of the compositions between the AIs and the matrix, Fig. 3c. Diffusion can also lead to a decreasing size temporally of AIs, Fig. 1b–d. To rationalize the size evolution of the AIs, we examine both the AIs and the matrix within the context of the Gibbs-Thomson effect [35–37]. The AIs are embedded in the M_7C_3 phase, thus the Al/ M_7C_3 interfaces have generally positive curvatures, while the interfaces between the M_7C_3 phase and the austenite matrix have much smaller curvature (see SI, Fig. S2 for a schematic). Therefore, as a result of the curvature-related Gibbs-Thomson effect, the equilibrium concentration of matrix atoms M just outside the AIs/ M_7C_3 interfaces is on average larger than that just inside the matrix/ M_7C_3 interface, and thus the AIs slowly disappear. Note the initially formed AIs are not particularly small (typically several hundred nanometers in diameter) due to the ample number of rejected solute atoms. Thus, the capillary effect (Ostwald ripen-

ing) is not very large. Therefore, the chemical potential of the AIs is only slightly larger than that of the matrix, leading to a small net atomic flux from the AIs to the matrix at this temperature. As a result, the AIs can be stable in size for a fairly long time, shrinking very slowly. At the depth of 200 μm , the $M_{23}C_6/M_7C_3$ transformation occurred at 14 h, based on the fitted kinetic parameters (reported separately [38]). After carburizing for 98 h (84 h after the initial AIs' nucleation at a depth of 200 μm) there are many AIs, although significantly smaller, remaining in the M_7C_3 carbides, Fig. 1b. Compared to the almost immediate nucleation and growth of the AIs (with the local $M_{23}C_6$ carbides supplying the solute atoms) during the $M_{23}C_6/M_7C_3$ transformation, the stability of the AIs inside the M_7C_3 carbide precipitates after the transformation is exceptional.

In summary, we investigated the formation of novel AIs within the carbide structures of an Fe-Ni-Cr-rich high-temperature alloy using a combination of multi-scale experimental techniques and thermodynamic calculations. The AIs are truly isolated structures, disconnected from the matrix, which nucleate during the

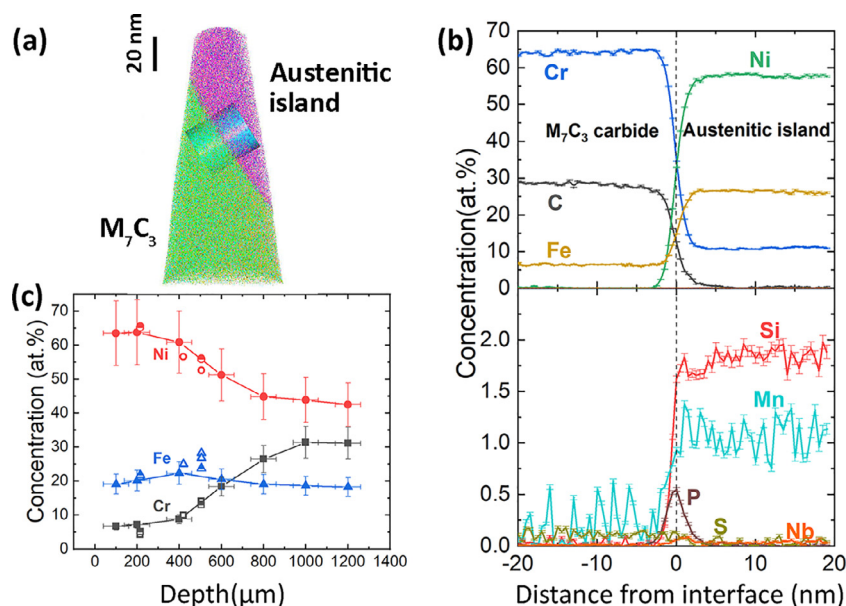


Fig. 3. (a) APT reconstruction of one nanotip, lifted at a depth of 505 μm , which captures the M_7C_3 phase and the Al. A cylindrically shaped region of interest (ROI) is displayed across the heterophase interface. (b) 1D concentration profiles of the alloying elements across the M_7C_3 /Al heterophase interface, along the z-axis of the cylindrically shaped ROI. (c) The concentrations of the major elements (Ni, Cr, Fe) of the Als measured by APT (open symbols), compared with matrix concentrations measured by both APT (half-filled symbols) and SEM EDS (filled symbols) at different depths.

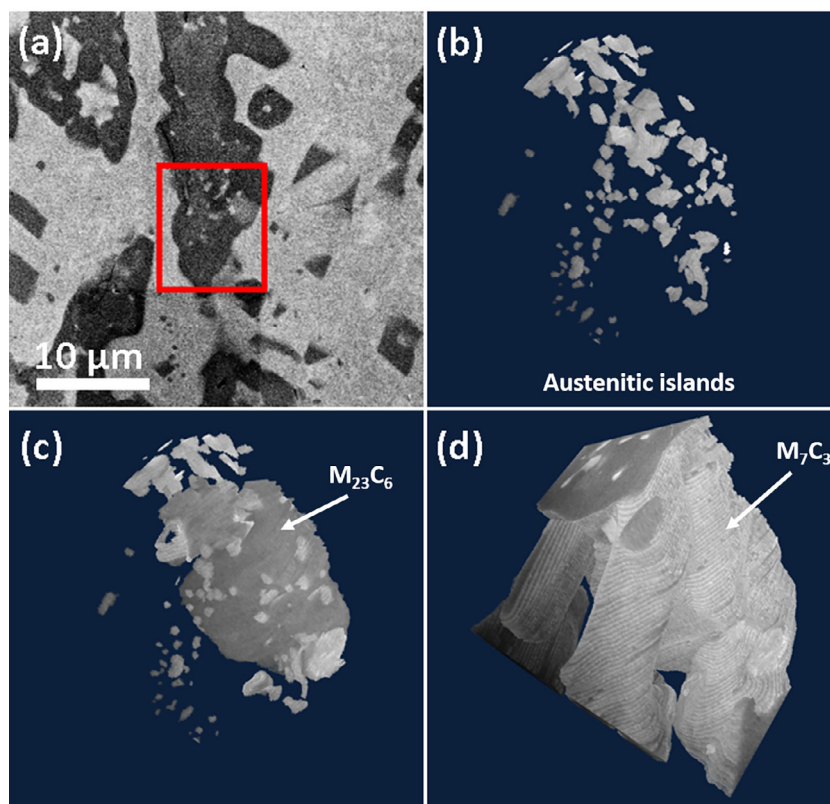


Fig. 4. (a) SEM micrograph of a selected carbide structure for FIB tomography. (b) Reconstruction displaying the Als only. (c) Reconstruction of Als and the $M_{23}C_6$ carbides. (d) Reconstruction of $M_{23}C_6$ carbides, and the M_7C_3 carbides. Note in the reconstruction, the original SEM contrast is preserved, and matrix austenitic phase is not shown for the sake of clarity. An animation that reveals the full 3D spatial relationship of the various structures can be viewed as a supplemental file in the online version of this article.

$M_{23}C_6$ / M_7C_3 transformation from solute atoms rejected from the M_7C_3 carbide which supersaturate $M_{23}C_6$ during the carburization process. The Als equilibrate their compositions with the matrix temporarily by elemental diffusion but are relatively stable to coarsening (Ostwald ripening) inside the carbides due to their large sizes.

Declaration of Competing Interest

MD, RZ, SD, RM and YD are employed by Dow Chemical Company which uses high temperature alloys in some of its chemical manufacturing operations.

Acknowledgment

This research was supported by Dow Chemical Company's University Partnership Initiative. This work made use of the EPIC facility of Northwestern University's NUANCE Center, which has received support from the Soft and Hybrid Nanotechnology Experimental (SHyNE) Resource (NSF ECCS-1542205); and the MRSEC program (NSF DMR-1720139) at the Materials Research Center. The LEAP tomograph at NUAPT was purchased and upgraded continuously with grants from the NSF-MRI program (DMR-0420532) and ONR-DURIP program (N00014-0400798, N00014-0610539, N00014-0910781, N00014-1712870) programs. Atom-probe tomography was performed at the Northwestern University Center for Atom-Probe Tomography (NUAPT). NUAPT received support from the MRSEC program (NSF DMR-1720139) at the Materials Research Center, the SHyNE Resource (NSF ECCS-1542205), and the Initiative for Sustainability and Energy (ISEN) at Northwestern University. The authors thank Dr. Qingqiang Ren of Northwestern University, currently at Oak Ridge National Laboratory, for valuable discussions.

Supplementary materials

Supplementary material associated with this article can be found, in the online version, at doi:[10.1016/j.scriptamat.2021.113792](https://doi.org/10.1016/j.scriptamat.2021.113792).

References

- [1] T.R. Allen, E.A. Kenik, G.S. Was, J. Nucl. Mater. 278 (2) (2000) 149–163.
- [2] H. Zhang, C. Li, Y. Liu, Q. Guo, H. Li, Mater. Sci. Eng. 677 (2016) 515–521.
- [3] T.D. Nguyen, J. Zhang, D.J. Young, Corros. Sci. 112 (2016) 110–127.
- [4] T.G. Lach, T.S. Byun, K.J. Leonard, J. Nucl. Mater. 497 (2017) 139–153.
- [5] Y. Zhong, X. Liu, K.-C. Lan, H. Lee, D.K.L. Tsang, J.F. Stubbs, Int. J. Fatigue 139 (2020) 105787.
- [6] Ethylene Market Share, Size, Trends, Industry Analysis Report By Feedstock (Naphtha, Ethane, Propane, Butane); By Application (Polyethylene, Ethylene Oxide, Ethyl Benzene, Ethylene Dichloride); By End-Use (Building & Construction, Automotive, Packaging, Textiles, Agriculture & Agrochemicals); By Region, Segment Forecast, 2020 - 2026, Polaris Market Research, 2020.
- [7] W. Herda, A. Rickard, Metallurgist 5 (7) (1973) 342–350.
- [8] E.A. Kenik, P.J. Maziasz, R.W. Swindeman, J. Cervenka, D. May, Scr. Mater. 49 (2) (2003) 117–122.
- [9] I.C. Silva, J.M.A. Rebello, A.C. Bruno, P.J. Jacques, B. Nysten, J. Dille, Scr. Mater. 59 (9) (2008) 1010–1013.
- [10] A.A. Kaya, Mater. Charact. 49 (1) (2002) 23–34.
- [11] D.J. Young, High Temperature Oxidation and Corrosion of Metals, first ed., Elsevier, Amsterdam, Boston, London, 2008 ed..
- [12] G.M. Smith, D.J. Young, D.L. Trimm, Oxid. Met. 18 (5) (1982) 229–243.
- [13] R. Petkovic-Luton, T.A. Ramanarayanan, Oxid. Met. 34 (5-6) (1990) 381–400.
- [14] R. Yin, Corros. Sci. 47 (8) (2005) 1896–1910.
- [15] S.J. Zhu, Y. Wang, F.G. Wang, J. Mater. Sci. Lett. 9 (5) (1990) 520–521.
- [16] A.A. Kaya, P. Krauklis, D.J. Young, Mater. Charact. 49 (1) (2002) 11–21.
- [17] S. Shi, J.C. Lippold, Mater. Charact. 59 (8) (2008) 1029–1040.
- [18] A.C. McLeod, C.M. Bishop, K.J. Stevens, M.V. Kral, Metallogr. Microstruct. Anal. 4 (4) (2015) 273–285.
- [19] R.P. Kolli, D.N. Seidman, Microsc. Microanal. 13 (4) (2007) 272–284.
- [20] S. Shu, B.D. Wirth, P.B. Wells, D.D. Morgan, G.R. Odette, Acta Mater. 146 (2018) 237–252.
- [21] E.A. Marquis, D.N. Seidman, Acta Mater. 49 (11) (2001) 1909–1919.
- [22] C. Monachon, M.E. Seidman, D.C. Dunand, Acta Mater. 59 (9) (2011) 3398–3409.
- [23] C. Monachon, D.C. Dunand, D.N. Seidman, Small 6 (16) (2010) 1728–1731.
- [24] G. Martin, P. Bellon, in: H. Ehrenreich, F. Spaepen (Eds.), Solid State Physics—Advances in Research and Applications, 50, Elsevier Academic Press Inc, San Diego, 1997, pp. 189–331.
- [25] B. Stumphy, R.S. Averback, P. Bellon, J. Mater. Res. 30 (2) (2015) 170–178.
- [26] S. Shu, P. Bellon, R.S. Averback, Phys. Rev. B 87 (14) (2013).
- [27] F. Vogel, N. Wanderka, Z. Balogh, M. Ibrahim, P. Stender, G. Schmitz, J. Banhart, Nat. Commun. 4 (1) (2013) 2955.
- [28] S. Meher, L.K. Aagesen, M.C. Carroll, T.M. Pollock, L.J. Carroll, Sci. Adv. 4 (11) (2018) eaao6051.
- [29] G. Song, Z. Sun, L. Li, X. Xu, M. Rawlings, C.H. Liebscher, B. Clausen, J. Poplawsky, D.N. Leonard, S. Huang, Z. Teng, C.T. Liu, M.D. Asta, Y. Gao, D.C. Dunand, G. Ghosh, M. Chen, M.E. Fine, P.K. Liaw, Sci. Rep. 5 (2015) 16327.
- [30] G. Lai, Warrendale, PA: TMSAIME (1985) 551.
- [31] M. Schaffer, B. Schaffer, Q. Ramasse, Ultramicroscopy 114 (2012) 62–71.
- [32] NbC Crystal Structure: Datasheet from "PAULING FILE Multinaries Edition - 2012" in SpringerMaterials (https://materials.springer.com/isp/crystallographic/docs/sd_0261185), in: P. Villars, K. Cenzual (Eds.) Springer-Verlag Berlin Heidelberg & Material Phases Data System (MPDS), Switzerland & National Institute for Materials Science (NIMS), Japan.
- [33] X.B. Hu, Y.L. Zhu, L.Z. Zhou, B. Wu, X.L. Ma, Philos. Mag. Lett. 95 (4) (2015) 237–244.
- [34] D.J. Larson, T.J. Prosa, R.M. Ulfig, B.P. Geiser, T.F. Kelly, New York, US: Springer Science (2013).
- [35] C.A. Johnson, Surf. Sci. 3 (5) (1965) 429–444.
- [36] M. Perez, Scr. Mater. 52 (8) (2005) 709–712.
- [37] M. Lin, G. Gottstein, L.S. Shvindlerman, Acta Mater. 129 (2017) 361–365.
- [38] M. Kazemzadeh-Atoufi, Unpublished data.